



Article

Carbon Fiber Polymer Reinforced 3D Printed Composites for Centrifugal Pump Impeller Manufacturing

Gabriel Mansour¹, Vasileios Papageorgiou¹ and Dimitrios Tzetzis^{2,*}

¹ Department of Mechanical Engineering, Aristotle University of Thessaloniki, 54124 Thessaloniki, Greece; mansour@auth.gr (G.M.); vasileiosp@meng.auth.gr (V.P.)

² Digital Manufacturing and Materials Characterization Laboratory, School of Science and Technology, International Hellenic University, 57001 Themi, Greece

* Correspondence: d.tzetzis@ihu.edu.gr

Abstract: Centrifugal pumps are used extensively in various everyday applications. The occurrence of corrosion phenomena during operation often leads to the failure of a pump's operating components, such as the impeller. The present research study examines the utilization of composite materials for fabricating centrifugal pump components using additive manufacturing as an effort to fabricate corrosion resistant parts. To achieve the latter two nanocomposite materials, carbon fiber reinforced polyamide and carbon fiber reinforced polyphenylene sulfide were compared with two metal alloys, cast iron and brass, which are currently used in pump impeller manufacturing. The mechanical properties of the materials are extracted by performing a series of experiments, such as uniaxial tensile tests, nanoindentation and scanning electron microscope (SEM) examination of the specimen's fracture area. Then, computational fluid dynamics (CFD) analysis is performed using various impeller designs to determine the fluid pressure exerted on the impeller's geometry during its operation. Finally, the maximum power rating of an impeller that can be made from such composites will be determined using a static finite element model (FEM). The FEM static model is developed by integrating the data collected from the experiments with the results obtained from the CFD analysis. The current research work shows that nanocomposites can potentially be used for developing impellers with rated power of up to 9.41 kW.

Keywords: additive manufacturing; mechanical properties; carbon fiber polymers; finite element analysis (FEA); computational fluid dynamics (CFD); centrifugal pump; impeller



Citation: Mansour, G.; Papageorgiou, V.; Tzetzis, D. Carbon Fiber Polymer Reinforced 3D Printed Composites for Centrifugal Pump Impeller Manufacturing. *Technologies* **2024**, *12*, 48. <https://doi.org/10.3390/technologies12040048>

Academic Editor: Eugene Wong

Received: 21 February 2024

Revised: 21 March 2024

Accepted: 29 March 2024

Published: 3 April 2024



Copyright: © 2024 by the authors. Licensee MDPI, Basel, Switzerland. This article is an open access article distributed under the terms and conditions of the Creative Commons Attribution (CC BY) license (<https://creativecommons.org/licenses/by/4.0/>).

1. Introduction

During the last decade, several types of additive manufacturing (AM) technologies, such as material extrusion, material jetting, powder bed fusion, etc., have been developed [1]. Such technologies allow us to use an assortment of materials, including metals, polymers, ceramics, and composites to fabricate three-dimensional objects [2–5]. In addition to the latter, additive manufacturing integrated with composites has even extended the capabilities of this technology further. Composite materials are made by fusing together two or more distinct components which possess distinct properties to produce a material with enhanced strength, durability, and other desirable characteristics [6,7]. The merging of composite materials and additive manufacturing has paved the way for fabricating lightweight, yet robust, structures that contain complex designs that were previously incredibly challenging to fabricate using traditional methods [8,9]. Fused filament fabrication (FFF) is one of the most used and affordable 3D printing techniques nowadays. FFF is a layer-by-layer additive manufacturing technology where a heated thermoplastic filament is extruded through a nozzle to construct physical parts from computer-aided design (CAD) via incremental material deposition [10–12]. AM has radically altered the way parts and products are designed and produced, enabling quicker, more cost-efficient production, as

well as the ability to produce complex and unique physical parts without the need for expensive tooling. This revolutionary technology is now utilized in a variety of fields, including aerospace, medical technology, and many others. At the present time, AM is used to fabricate end-use parts in addition to prototyping and concept product creation [13,14]. Fabricating water pump impellers is an example of the utilization of AM to produce end-use components. The construction material of an impeller varies for centrifugal pumps, and it is based on the application and operating conditions. Impellers are usually manufactured primarily from metal alloys, cast iron as illustrated in Figure 1, stainless steel, or bronze. In smaller-scale centrifugal pump designs, aluminum and plastic polymers are also used as construction materials [15].

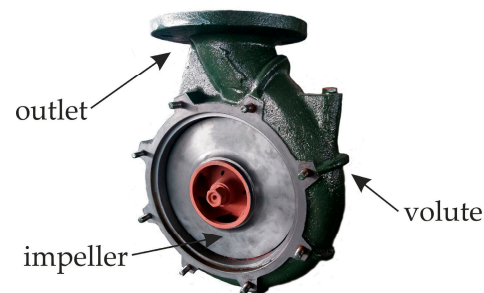


Figure 1. Centrifugal pump with a cast iron impeller.

The main issue encountered during the operation of centrifugal pumps is the corrosion-induced wear of the metal functional components [16,17]. This kind of wear reduces the impeller's hydraulic efficiency. The impeller's surface can be affected by several types of corrosion, including stress corrosion fracture, cavitation, and corrosion fatigue [18,19]. In a comparison between the two impellers illustrated in Figure 2, the new one and the worn one, signs of corrosion erosion at the impeller's hub and shroud are evident. Additionally, corrosion due to cavitation on the blade's leading and trailing edges has been detected. Near the impeller's inlet diameter these corrosion phenomena resulted in a significant crack which can lead to the impeller's failure. To mitigate the evident corrosion related effects and reassure the hydraulic efficiency of the turbomachinery component, composite materials in conjunction with additive manufacturing (AM) technologies can be utilized for the fabrication of impellers. This research aims to investigate the use of composite materials in conjunction with AM technology to fabricate a prototype 3D printed composite impeller. The prototype impeller must meet the mechanical specifications required for proper operation in a water pump.

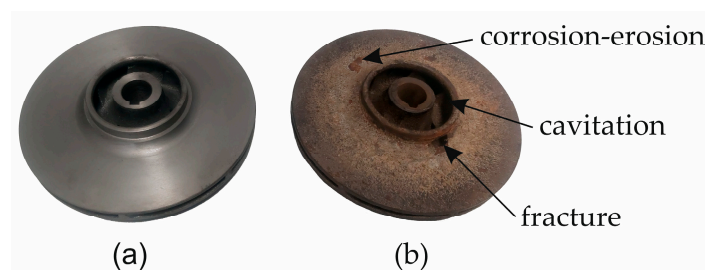


Figure 2. Cast iron impellers: (a) new impeller, (b) impeller after five hundred hours of operation.

A considerable number of studies have been conducted regarding the development and fabrication of centrifugal impellers using fused filament fabrication (FFF) AM technology which meet the mechanical specifications and the desired hydraulic efficiency. Various polymer specimens were tested in tensile and bending conditions to determine if they could fulfil the functional requirements of a centrifugal pump impeller [20]. S. Fernández et al. [21] manufactured an FFF impeller replicated from the original one provided by the

manufacturer of the pump. The FFF impeller has been tested in operating conditions to evaluate its overall performance in comparison with the original one. Due to the reduced surface roughness that can be achieved through AM, the FFF impeller exhibits an increase in efficiency of approximately 2%. In addition, the experimental results demonstrated that the AM impeller is approximately one-third less expensive than its metal counterpart. In another work, Nelson S. Andres [22] developed an AM impeller to be used in a solar powered water pump to achieve lower energy consumption. According to measurements and calculations, the power consumption of the pump with a plastic impeller was determined to be less than that of the pump with a metal impeller. When the AM plastic impeller replaced the water pump's original metal impeller, the current decreased by 15.38%. Furthermore, the AM plastic impeller was found to be reliable and rigid enough to perform the same function as a conventional metal impeller after more than 300 h of testing. Additionally, the reconstruction of a broken centrifugal impeller was successfully carried out using additive manufacturing as reported by N. Kladovasilakis et al. [23]. As the deviations of the printed impeller were relatively minor, the results demonstrated that the repair of functional spare parts could be accomplished via AM with high dimensional accuracy. As a technologically and environmentally friendly manufacturing method, fused filament for fabrication created from recycled plastic has been used by Heshan Jayawardane et al. [24] to fabricate semi-open water pump impellers. Due to its lower density, ultimate tensile strength, and fatigue strength in comparison to the virgin polylactic acid (VPLA) material, the recycled PLA (RPLA) impeller's estimated service life was reduced. The RPLA impeller had substantially higher (74%) life cycle costs. Nonetheless, the RPLA impeller produces 93% less environmental impact than the VPLA impeller. Added to the latter research, computational fluid dynamic (CFD) analysis has also been conducted on a centrifugal pump impeller to calculate and enhance the overall performance and the efficiency of the impeller [25–27]. Also, a CFD analysis has been conducted to calculate the velocity and pressure contour alongside the blade of the impeller as well as the cavitation phenomenon which causes significant loss of performance and degradation of life in the centrifugal pumps [28–30].

The current research aims to examine and contrast the traditional materials used in the fabrication of impellers with the composite ones built utilizing the FFF additive manufacturing technology. The mechanical properties of four materials were tested, two metal alloys, currently used for impeller manufacturing, and two carbon fiber composite filaments. The specimens were subjected to uniaxial tensile and nanoindentation tests. A scanning electron microscope (SEM) was also used to assess the morphology of the materials under study. An essential objective is to determine the maximum power the impeller's geometry can withstand without breaking. A computational fluid dynamic (CFD) analysis was performed to determine the pressure and velocity profile of the impeller, while a static model evaluated the overall performance of the impeller under stress conditions for the materials used.

2. Materials and Methods

2.1. Materials

The materials which will be tested are a cast iron alloy, a brass alloy, 15% carbon fiber reinforced polyamide 6 (Spectrum PA6-CF15, Spectrum Filaments, Pęcice Małe, Poland), as well as 15% carbon fiber reinforced polyphenylene sulfide (PPS) (Treed PPS-CF15, TreeD Filaments, Seregno, Italy). Both cast iron and brass alloys are widely used for impellers and other centrifugal pump components, sand casting such as shells, bearing bases and others. All the specimens were fabricated according to standard BS EN 10002-1 [31] as illustrated in Figure 3. Sand casting was used for the fabrication of the cast iron alloy and the brass alloy specimen. The metal specimen's molds were created according to the latter standard and printed on a 3D printer in PLA (polylactic acid) accounting for shrinkage during casting (1% for cast iron alloy and 1.2% for the brass alloy one). The Raise-3D Pro 2 (Raise 3D Technologies, Inc., Irvine, CA, USA) 3D printer was used for both the molds and

the composite specimen fabrication along with the manufacturer's slicer software. Because composite filaments are extremely abrasive, a 0.80 mm hardened nozzle was used for their fabrication. The printing parameters used for the composite filament fabrication were chosen according to the filament manufacturer's recommendations [32,33]. As depicted in Table 1, both composite filaments provide high continuous working temperature while the water absorption is kept in very low percentages, lower than 0.3%. These characteristics, in addition to the materials' increased strength, allow for their utilization in a variety of turbomachinery applications.

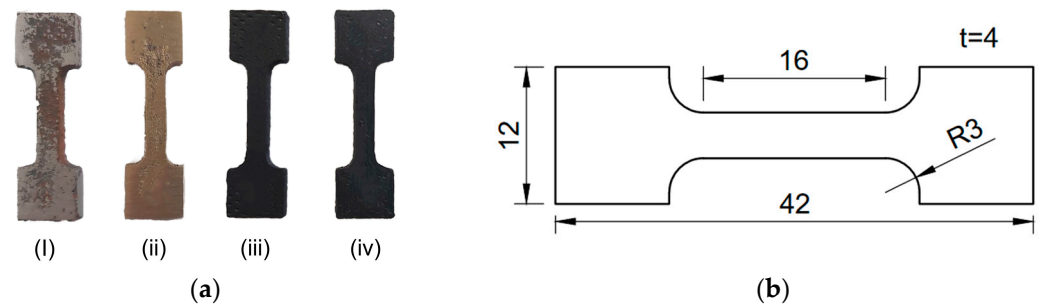


Figure 3. (a) Tensile specimen: (i) cast iron, (ii) brass alloy, (iii) PA6-CF15, (iv) PPS-CF15; (b) specimen dimensions.

Table 1. Physical properties of composite filaments.

Physical Properties	PA6-CF15	PPS-CF15
Heat distortion temperature (HDT)	200 °C	220 °C
Continuous service temperature	150 °C	220 °C
Coefficient of thermal expansion	$0.4 \times 10^{-5}/\text{K}$	$3 \times 10^{-5}/\text{K}$
Linear mold shrinkage	0.00–0.1%	0.2–0.5%
Water absorption, 23 °C/24 h	<0.3%	<0.05%
Specific gravity	1.25 g/cm ³	1.49 g/cm ³

For the PA6-CF15 specimen, the nozzle temperature was set at 280 °C, the heated bed temperature at 90 °C with 0.2 mm layer height, 100% concentric infill ratio, and 60 mm/s printing speed. For the PPS-CF15 specimen, the nozzle temperature was set at 310 °C, the heated bed temperature at 100 °C with 0.2 mm layer height, 100% concentric infill ratio, and 60 mm/s printing speed. Both composite filaments were dried at 90 °C for 4 h before printing to reassure the best overall mechanical properties of the filaments. Three specimens were fabricated per material to ensure satisfactory results from the experimental procedure.

2.2. Mechanical Testing

Each specimen was subjected to uniaxial tension to determine the material's ultimate tensile strength. For the uniaxial compression experiment, a universal mechanical testing machine (Testometric M500-50 AT, Rochdale, UK) was utilized and was equipped with a 50 kN load cell. The uniaxial test was conducted at a 5 mm/min crosshead speed and a 5 N tensile preload. Nanoindentation tests were also performed on samples of the materials under study. Testing of the samples was carried out using a Dynamic Ultra Micro Hardness Tester DUH-211S (Shimadzu Corp., Tokyo, Japan). A Berkovich diamond indenter with a 100 nm tip radius and a resolution of 0.196 μN penetrated the test surface with a specified load of 300 mN. The Oliver–Pharr [34,35] formula was utilized to compute

the elastic modulus and the hardness of the specimens under study. The hardness (H) can be calculated as a function of the maximum penetration depth of the indentation:

$$H = \frac{P_{max}}{A} \quad (1)$$

where P_{max} is the maximum applied load measured at the maximum depth of penetration (h_{max}) and A is the projected contact area between the indenter and the film. For a perfect Berkovich indenter, value A can be expressed as a function of the contact indentation depth h_f as:

$$A = 3\sqrt{3}h_f^2 \tan^2 65 = 23.96h_f^2 \quad (2)$$

The contact indentation, h_f , can be determined from the following expression:

$$h_f = h_{max} - \varepsilon \frac{P_{max}}{S} \quad (3)$$

where ε is a geometric constant $\varepsilon = 0.75$ for a pyramidal indenter and S is the contact stiffness that can be determined as the slope of the unloading curve at the maximum loading point, i.e.,

$$S = \left(\frac{dP}{dh} \right)_{h=h_{max}} \quad (4)$$

The reduced elastic modulus E_r is given by:

$$E_r = \frac{S}{2\beta} \sqrt{\frac{\pi}{A}} \quad (5)$$

where β is a constant that depends on the geometry of the indenter. For the applied Berkovich indenter, the parameter β was equal to 1.034. The specimen elastic modulus (E_s) can then be calculated as:

$$\frac{1}{E_r} = \frac{1 - \nu_s^2}{E_s} + \frac{1 - \nu_i^2}{E_i} \quad (6)$$

where $E_{i,s}$ and $\nu_{i,s}$ are the elastic modulus and the Poisson's ratio for the indenter and the specimen, respectively. Moreover, for a diamond indenter, E_i is 1140 GPa and ν_i is 0.07. The specimen's hardness H and elastic modulus E_s were computed from the set of equations documented above.

3. Results

3.1. Mechanical Property and Fracture Morphology

Figure 4 illustrates the stress–strain diagram of each material. Brass alloy specimens showed the highest elongation and stress prior to fracture, with 40.37% elongation and 411.125 MPa tension. Cast iron demonstrated the second-highest tensile strength with 314.53 MPa tension and 20.225% strain. The PA6-CF15 specimens demonstrated 150.48 MPa stress tension and 2.19% strain, while PPS-CF15 specimens showed 79.8 MPa stress and 1.32% strain. As anticipated, the 3D printed specimens using FFF technology materials are inferior compared to metallic ones. However, it can be observed that carbon fiber reinforced filaments [36,37] have higher strength than conventional composites used in additive manufacturing processes. PA6-CF15 has a tensile strength that is less than two and a half times when compared to cast iron. When operating stresses do not exceed its yield strength, this material could replace cast iron as construction material in the fabrication of specific components.

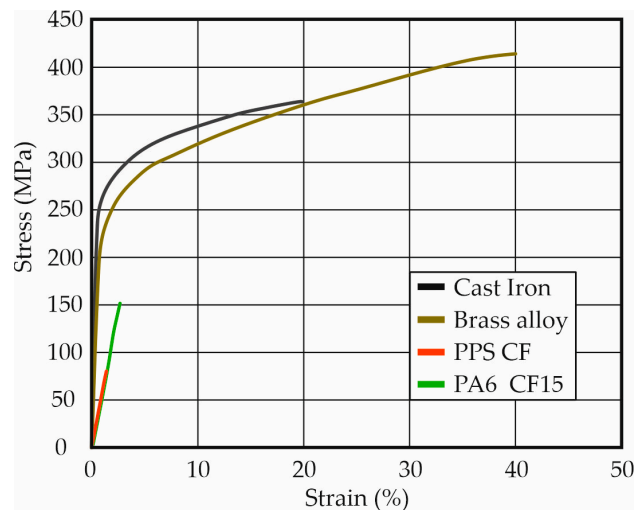


Figure 4. Uniaxial tensile stress–strain diagrams.

The typical load–depth curves of the printed PA6-CF15, PPS-CF15, cast iron, and brass alloy specimens from the nanoindentation tests are shown in Figure 5. The load–depth curves were obtained during the loading and unloading of the indenter. The composite specimen demonstrated creep at a peak load of 300 mN, as is illustrated in their nanoindentation load–depth curves. There were no discontinuities or step loading observed on the curves, indicating that no fractures formed during the nanoindentation process. Furthermore, the maximum indentation depths at the peak load of 300 mN varied approximately between 1.55 and 11 μm . The highest indentation depth was observed in the PA6-CF15 specimen where the indentation reached an average depth value of 11 μm .

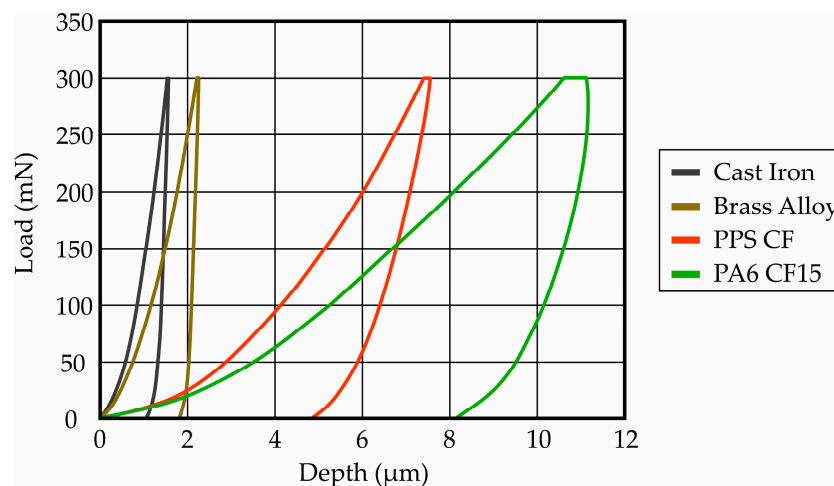


Figure 5. Load–depth curves of cast iron, brass alloy, PA6-CF15, and PPS-CF15.

The PPS-CF15 specimen showed an average indentation depth of 7.5 μm and the brass alloy specimen a depth of 2.24 μm . As anticipated, the cast iron specimens with a mean depth of 1.55 μm exhibited the lowest indentation depth, showing the highest indentation resistance for the given maximum load among the specimens tested. The indentation modulus was also calculated for each type of specimen, where the metal alloys showed the greater elastic modulus equal to 216 GPa and 108 GPa for the cast iron and brass alloy, respectively. On the other hand, the composite specimen exhibited an average elastic modulus equal to 4.57 GPa for the PA6-CF15 specimens and 5.13 GPa for the PPS-CF15 ones.

The mechanical properties measured are summarized in Table 2. The brass alloy showed higher strength than cast iron with values of 411.25 MPa against 314.53 MPa, as well as higher strain with values of 40.37% and 20.225% for the brass alloy and cast iron, respectively. Furthermore, cast iron showed a greater modulus of elasticity of 218 MPa with a hardness of 613.17 HV, whereas bronze demonstrated a modulus of elasticity of 108 MPa with a hardness of 238.33 HV. In terms of the materials studied, the PA6-CF15 reinforced with carbon fibers showed greater fracture resistance than the carbon fiber reinforced PPS-CF15. Due to the high content of carbon fibers in their polymer matrix, both composite materials showed brittle fracture. The difference in modulus of elasticity and hardness between the two materials is due to their distinct polymer matrix, polyamide 6 and polyphenylene sulfide. The modulus of elasticity was calculated as 4.57 GPa and a hardness stands at 13.72 MPa for PA6-CF15, while for PPS-CF15 the modulus of elasticity and the hardness were measured at 5.13 GPa and 26.16 MPa, respectively. Metal alloys exhibit almost the same behavior. Bronze has the highest strength though it shows the lowest hardness. Composite materials are considerably inferior to metal alloys in terms of strength and hardness. To ensure the functional component's resistance in operating conditions, when carbon fiber reinforced composites are used as construction materials rather than the metal alloys, a deeper analysis of the forces exerting on the component under study is mandatory.

Table 2. Tensile and nanoindentation test results.

Material	Tensile Strength (MPa)	Tensile Yield Strength (MPa)	Strain (%)	Modulus of Elasticity (GPa)	Hardness (MPa)
Cast iron	314.53	235	20.225	216	613.17
Brass	411.25	210	40.37	108	238.33
PA6-CF15	150.48	140	2.19	4.57	13.72
PPS-CF15	79.8	70	1.32	5.13	26.16

The morphology of both the composite and the metal samples was examined by the scanning electron microscopy (SEM) technique using a scanning electron microscope (SEM). The fractured surfaces of the cast iron specimens reveal characteristic brittle cracks with some river-like lines, as depicted in Figure 6a. These cracks likely originated from specimen detachment and the presence of micro gas cavities. In Figure 6b, the general fracture pattern of the brass suggests a brittle failure mode, accompanied by numerous secondary microcracks. The brass structure exhibits evenly distributed bright lead particles. It is noteworthy that the tensile strength enhancement in composites is influenced by factors such as the dispersion of fibrous filler in the matrix and the adhesion between the fiber and matrix interface. This phenomenon is clear in the SEM micrographs of both composite materials under study. In the case of PPS-CF15 composites (Figure 6c), the fiber surfaces appear smooth and clean, with voids between the fiber and matrix due to debonding, indicating weak adhesion between carbon fibers and PPS matrix. Some larger voids could be due to moisture. In contrast, carbon fibers in the PA6 matrix (Figure 6d) are well-distributed, and despite undergoing tensile testing, most carbon fibers exhibit strong adhesion to the matrix, contributing to the overall improvement in the composite's tensile strength.

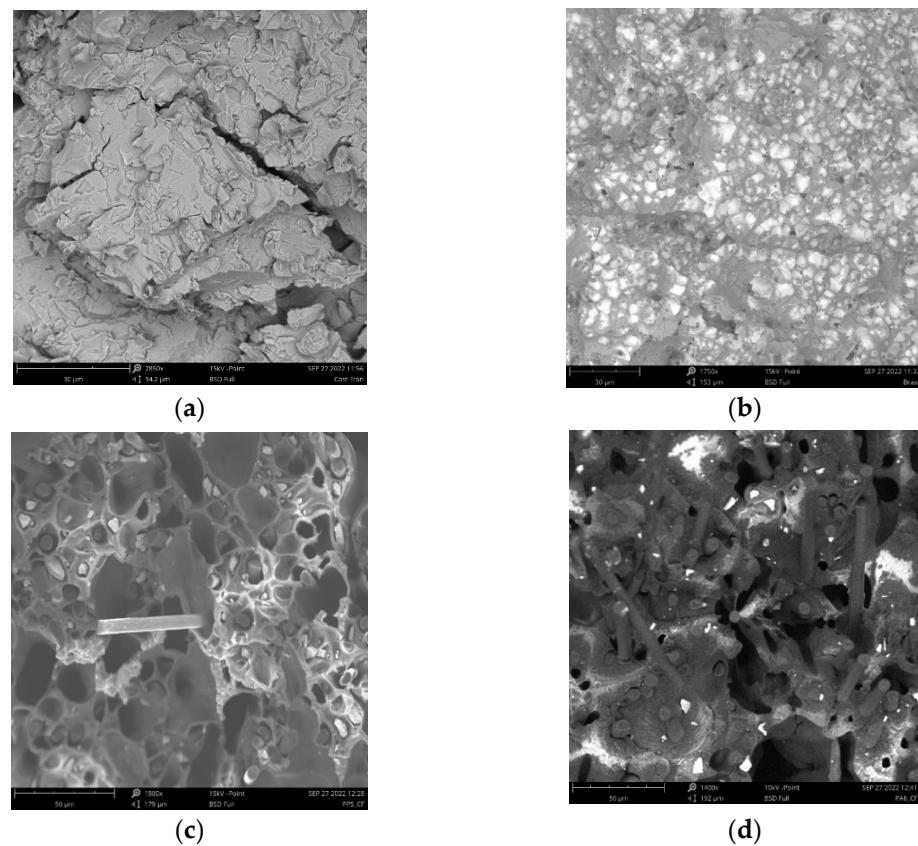


Figure 6. Specimen fracture area: (a) cast iron, (b) brass alloy, (c) PPS-CF15, (d) PA6-CF15.

3.2. Computational Fluid Dynamics of an Impeller

To study the construction of a closed-type impeller made of composite materials using additive manufacturing, it is required to first calculate the pressure exerted on the impeller by the fluid during operation. Considering the overall geometry of a closed-type impeller, the greatest pressures exerted on its body are situated on the impeller's trailing edge. The trailing edge, along with the keyway, through which torque is transmitted from the shaft, are the critical failure points of the overall geometry. The study was conducted entirely in Ansys software 2022R2 (ANSYS, Inc., Canonsburg, PA, USA). The impeller was initially designed using Vissta CPD, which employs a 1D approach for the preliminary design of the centrifugal impeller. The design assumptions and input parameters are illustrated in Tables 3 and 4.

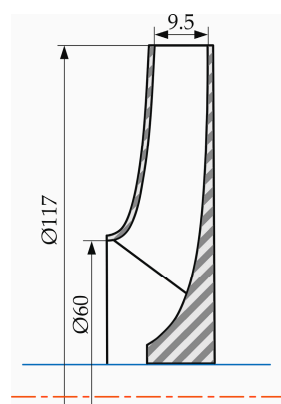
Table 3. Initial input parameters for the CFD study.

Input Parameter	Symbol	Value
Volume flow rate	Q [m^3/h]	25
Head rise	H [m]	17
Power	P [kW]	1.492
Rotational speed	N [rpm]	2900
Inlet flow angle	θ_1 [degree]	90
Hydraulic efficiency	η_H	0.87
Volumetric efficiency	η_V	0.97
Mechanical efficiency	η_m	0.95
Pump efficiency	η_p	0.8

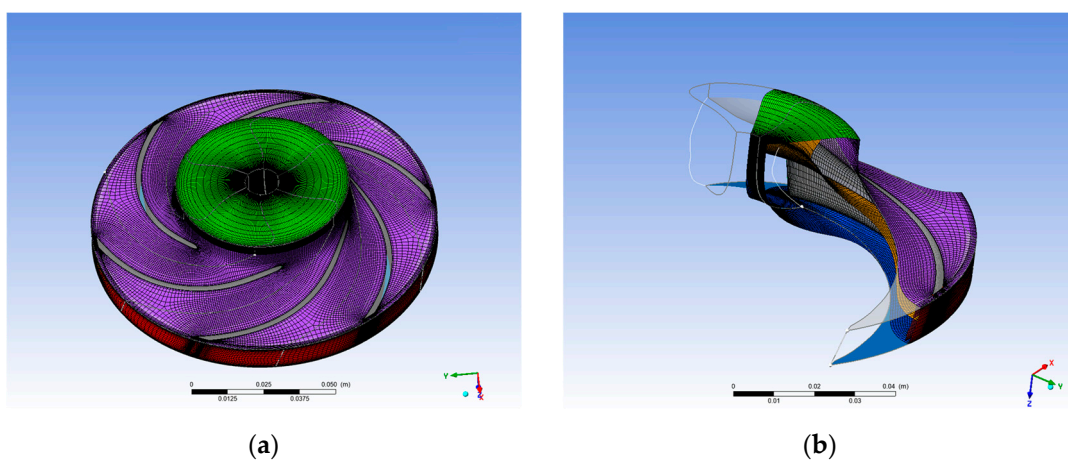
Table 4. Impeller design assumptions.

Assumptions	Symbol	Value
Shaft min diameter safety factor	D_f^{\min}	1.2
Hub to shaft diameter ratio	$\frac{D_{hub}}{D_{shaft}}$	1.5
Hub inlet draft angle	β_1 [degree]	30°
Blade angle at exit	β_2 [degree]	22.5°

The impeller design was completed in the Blade Generator. In this design phase, the nominal layer thickness was set from the leading edge through the trailing edge of the impeller as well as the theta and beta angles of the blade. The final impeller design dimensions are illustrated in Figure 7, where the inlet diameter was chosen as 60 mm, the exit diameter 117 mm, the exit width 9.5, and the number of blades was 6.

**Figure 7.** Impeller characteristic dimensions.

The impeller geometry as well as the inlet, outlet, low-periodic, and high-periodic surfaces were meshed in turbogrid. The final mesh consisted of 115,500 elements (Figure 8a). The impeller is a symmetrical component. Therefore, for the convenience and greater accuracy of the subsequent computational simulations, only one section was isolated from the impeller's overall geometry, as illustrated in Figure 8b.

**Figure 8.** (a) Final impeller mesh, (b) Single blade mesh.

The density of the fluid, the rotational speed, the inlet pressure of the fluid, and the mass flow rate in the outlet were established for the analysis. Figure 9a illustrates the pressure distribution along the blade under operational conditions. The analysis results

indicate that the maximum pressure exerted across the impeller's geometry does not surpass 0.3 MPa. The pressure increases closer to the trailing edge of the blade. The area around the blade's trailing edge constitutes a possible fracture area. In Figure 9b the fluid's velocity across the blade is illustrated. In conjunction with the previous figure, as the fluid's velocity increases, so does the pressure exerted by the fluid on the impeller blade. The designed impeller produced 17 mH₂O head pressure at 25 m³/h mass flow rate while utilizing 1.243 kW of power, according to the findings of the CFD analysis. The design's overall efficiency is 95.77%.

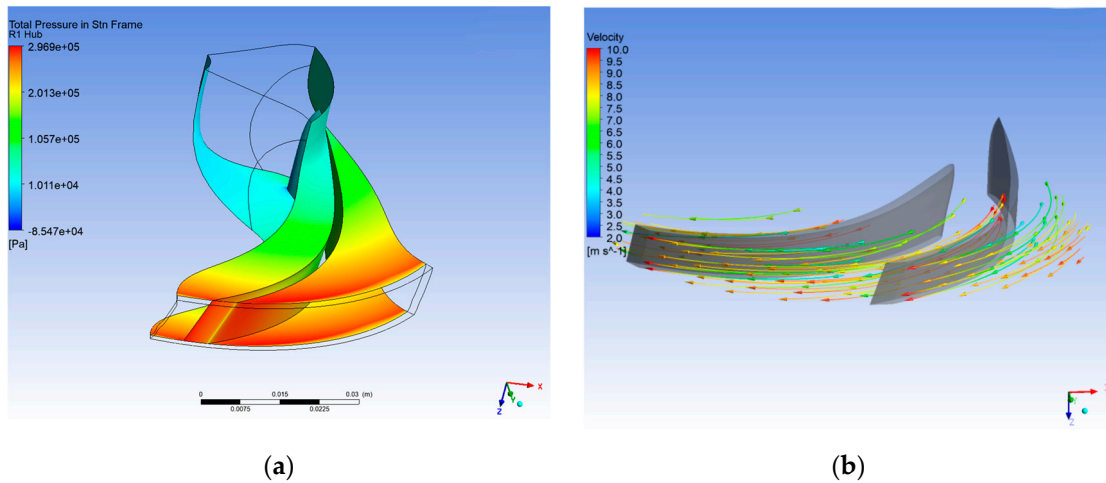


Figure 9. (a) Pressure distribution along the impeller, (b) velocity streamlines along the blade.

3.3. Impeller Structural Analysis

Calculating the elastic stresses developed on the impeller during operation requires knowledge of the pressure profile exerted on the blade by the fluid. By simulating the stresses exerted on the impeller in conjunction with its geometry and its construction material, both the equivalent stress and strain of the impeller under the specified operating conditions can be simulated as well. Figure 10a depicts the equivalent stress along the component. The greatest equivalent stress, 26.52 MPa, is recorded near the trailing edge of the blade as shown in Figure 10b. The average equivalent stress along the blade's geometry is approximately 10 MPa.

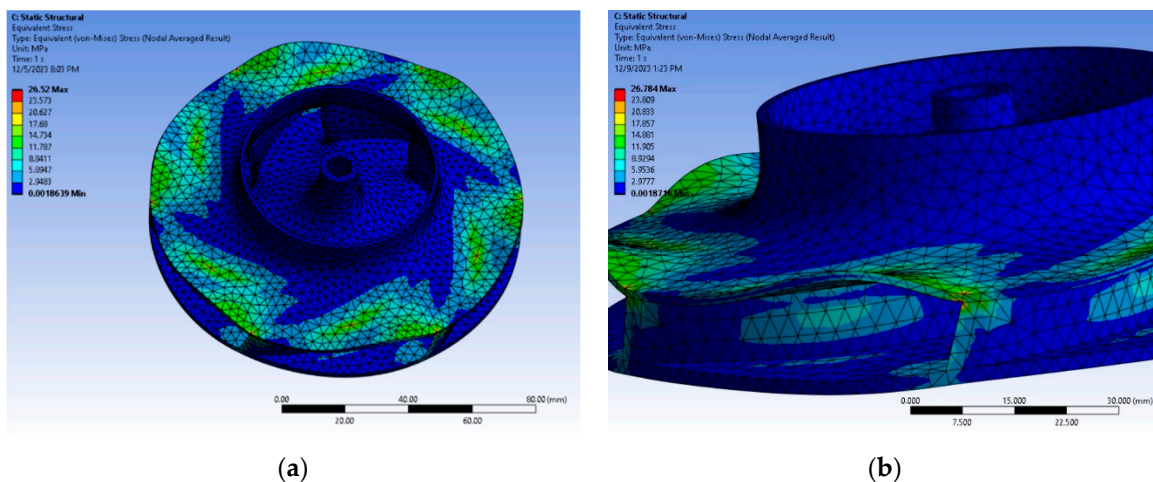


Figure 10. (a) Equivalent stress across the impeller, (b) critical stress area.

The calculated equivalent stress is much lower than the yield strength of both the metal alloys and the composite materials. The impeller's equivalent strain can be estimated

by inserting the construction material and its mechanical properties, as examined in the previous sections. As mentioned, the impeller manufacturing materials used nowadays are either brass alloys or cast iron. Figure 11a,b illustrates the equivalent elastic strain of the cast iron and brass alloy impellers. The equivalent strain computed for the cast iron impeller was 3.8×10^{-4} mm/mm, which was comparable to the corresponding strain calculated for the brass impeller, which was 4×10^{-4} mm/mm. In the case of composite materials, as shown in Figure 11c,d, the anticipated strain is 8×10^{-3} mm/mm when PA6-CF15 is chosen as the impeller's construction material, and 7×10^{-3} mm/mm when PPS-CF15 is used in its place. Both composite materials are appropriate for usage, according to the static structural study results for the specific impeller design. The computed equivalent strain for every single construction material did not exceed the yield stress of the material.

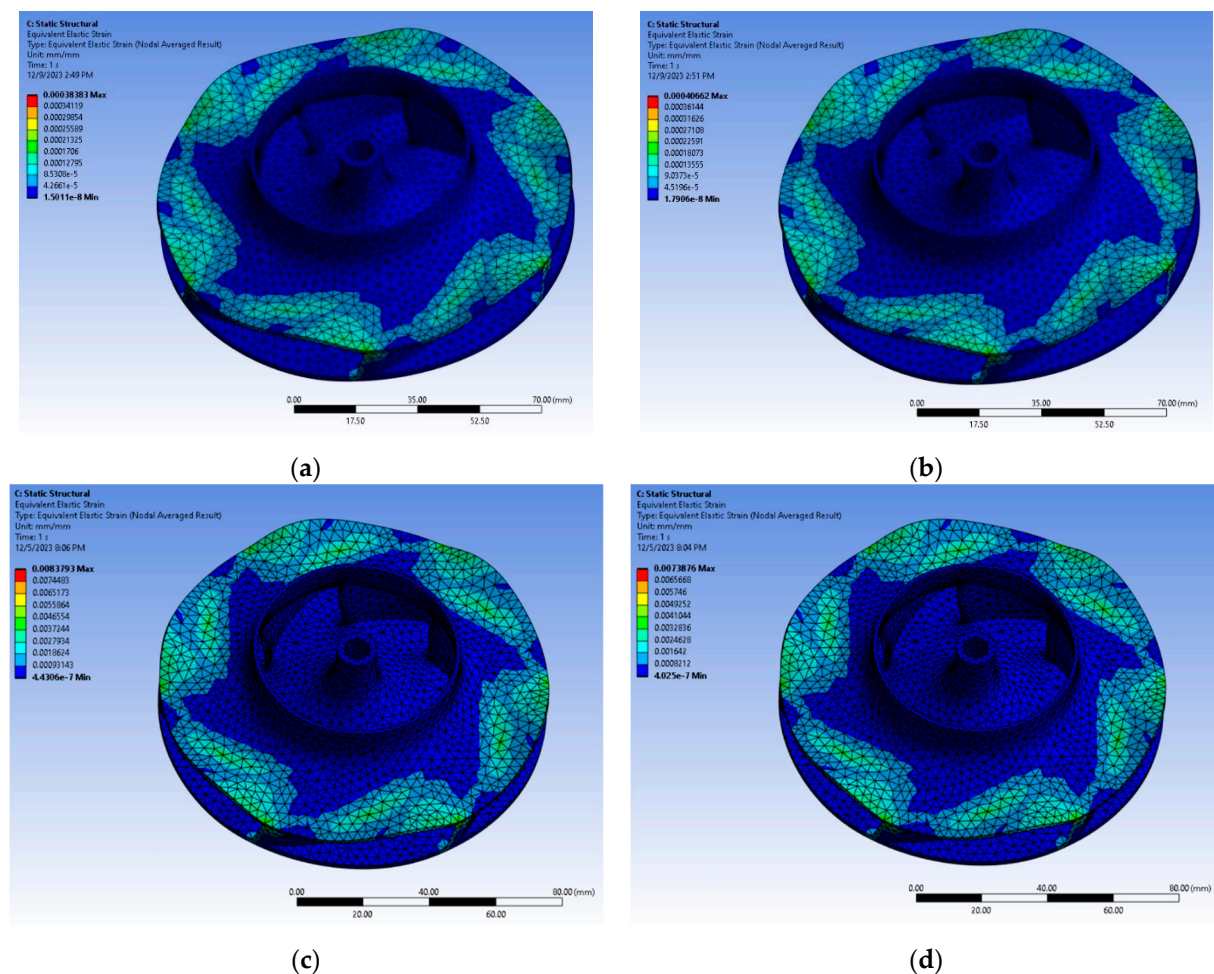


Figure 11. Equivalent strain: (a) cast iron impeller, (b) brass alloy impeller, (c) PA6-CF15 impeller, (d) PPS-CF15 impeller.

The maximum horsepower that a composite impeller can resist can be determined by repeating the latter calculation procedure and increasing the nominal horsepower of the design each time. The nominal power data to be tested matches the available power of the electric motors present. Table 5 summarizes the characteristics of the designs studied in further detail.

Table 5. Characteristics of the designs studied per impeller nominal power.

Impeller Nominal Power (kW)	Inlet Diameter (mm)	Outlet Diameter (mm)	Blade Height (mm)	Mass Flow (m ³ /h)	Head (m)	Number of Blades
4.1 kW	73	183	10.5	40	30	6
5.59 kW	77	175	11.5	42	35	6
7.46 kW	84.5	177	13	55	40	6
9.32 kW	88	193	13.5	55	48	6

The calculation and design of each model, the meshing process, and the determination of the boundary conditions for the CFD analysis are completed using the same methodology as the initial study. The results of the CFD study for each design are summarized in Table 6.

Table 6. CFD study results per impeller studied.

Calculated Power (kW)	Mass Flow (m ³ /h)	Calculated Head (m)	Total Efficiency (%)	Number of Elements
4.089	40	36.32	95.42	203,310
5.528	42	46.62	93.68	219,294
7.348	55	47.53	94.66	210,654
9.109	55	58.07	94.2	408,986

The estimated equivalent stresses for each nominal power impeller design during the static analysis are shown in Figure 12a–d. The maximum equivalent stress for the 4.1 kW impeller was 62.351 MPa, with an average stress of 35 MPa. The 5.59 kW impeller had a maximum equivalent stress of 80.026 MPa and an average stress of 40 MPa, whereas the 7.46 kW impeller had a maximum equivalent stress of 103.59 MPa and an average stress of 52 MPa. Also, the 9.32 kW impeller had a maximum equivalent stress of 116.24 MPa and an average stress of 64.5 MPa.

The highest tensile strength of the composite materials used in this study was 150.48 MPa for the PA6-CF15 and 79.8 MPa for the PPS-CF15. Accounting for a safety factor of 1.2 for the impeller designs, the maximum equivalent stress that each composite material can withstand is 120.38 MPa for the PA6-CF15 and 63.84 MPa for the PPS-CF15. Thus, the maximum impeller design that can be fabricated with PPS-CF15 is the 4.1 kW impeller, while the greatest impeller design that can be fabricated with PA6-CF15 is the 9.32 kW design. The equivalent strain for each material and maximum power design can be viewed in Figure 13a,b. The equivalent strain of the 4.1 kW design fabricated with PPS-CF15 is 0.016 mm/mm while the strain of the 9.32 kW impeller fabricated with PA6-CF15 is 0.028 mm/mm.

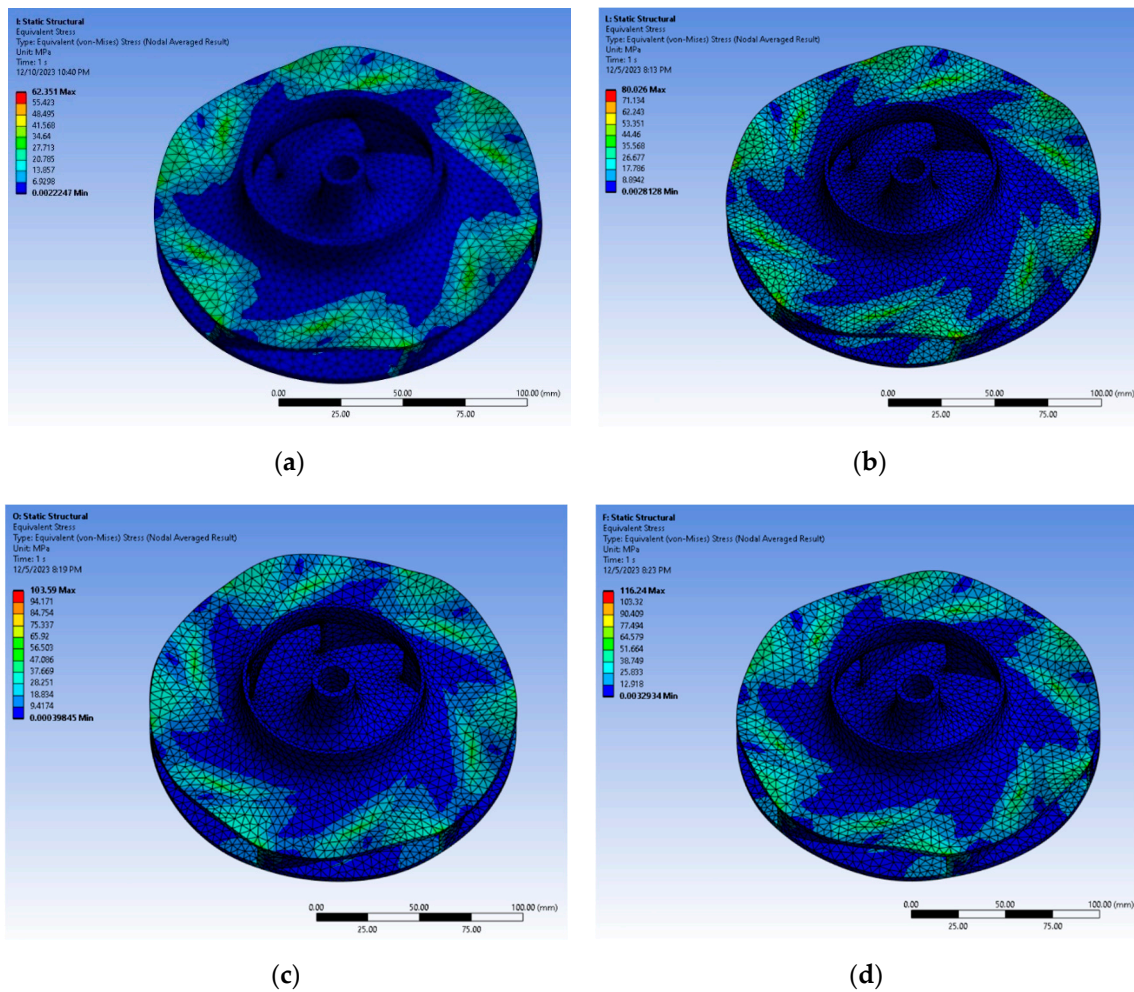


Figure 12. Equivalent stress: (a) 4.1 kW impeller, (b) 5.59 kW impeller, (c) 7.46 kW impeller, (d) 9.32 kW impeller.

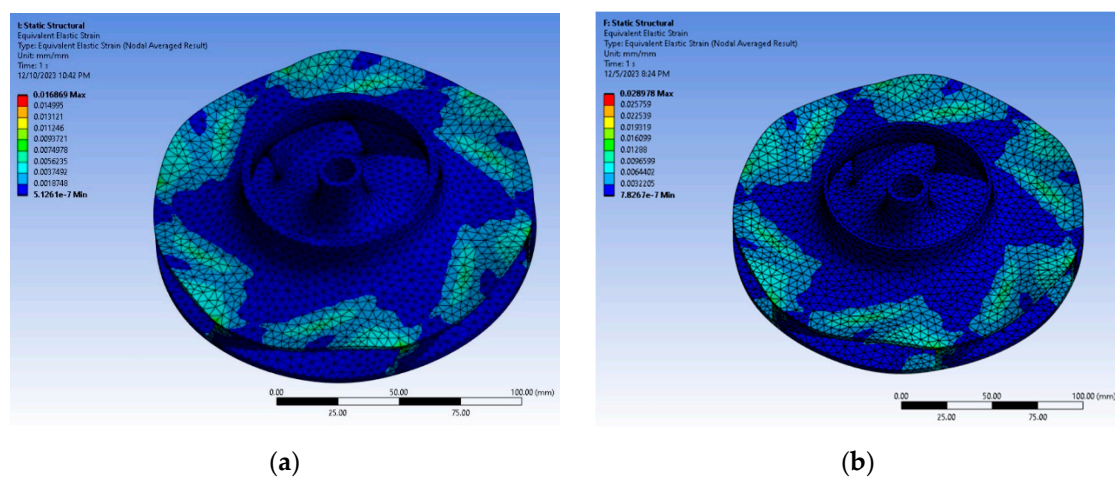


Figure 13. Equivalent strain of: (a) PPS-CF15 4.1 kW design, (b) PA6-CF15 9.32 kW design.

4. Conclusions

In the present study, the mechanical properties of several materials were analyzed to determine, via simulation, whether they are suitable for use in the construction of centrifugal pump impellers. After completing the tensile and nanoindentation tests, the modulus

of elasticity, ultimate and yield strength of each material were determined accordingly. By using a scanning electron microscope to examine the specimens, it was possible to identify vital information regarding the fracture patterns of each material. With the subsequent development of a CFD model of an impeller, the stresses exerted on the impeller's geometry during operation were simulated. The operational equivalent stresses and the corresponding equivalent strain per construction material were determined satisfactorily by developing an FEA model. Finally, both composite materials have been found to be appropriate for operation at a variety of power impeller ratings. The PA6-CF15 composite material was approved for operation up to 9.32 kW nominal maximum power, whereas the PPS-CF15 attained a maximum of 4.1 kW. However, composite materials cannot withstand the corresponding maximum load the metal materials can; but composite impellers are devoid of corrosion and consequently free of corrosion-induced wear phenomena such as corrosion erosion and corrosion fatigue. Furthermore, the composite materials tested in this study have low water absorption rate and they are also highly chemically resistant, making them appropriate for a variety of centrifugal pump designs, including those used in the chemical industry. In conclusion, this study report accomplished a sufficient preliminary analysis to investigate alternate contemporary impeller manufacturing methods and materials for use in hydrodynamic and rotodynamic applications.

Author Contributions: Conceptualization, G.M. and V.P.; methodology, G.M. and V.P.; software, V.P.; validation, V.P.; formal analysis, V.P.; investigation, V.P.; resources, V.P.; data curation, V.P.; writing—original draft preparation, V.P.; writing—review and editing, V.P., G.M. and D.T.; supervision, G.M. and D.T. All authors have read and agreed to the published version of the manuscript.

Funding: This research received no external funding.

Institutional Review Board Statement: Not applicable.

Informed Consent Statement: Not applicable.

Data Availability Statement: The datasets presented in this article are not readily available because the data are part of an ongoing study.

Acknowledgments: The authors would like to thank Chrysafi Pumps for providing technical information about the centrifugal pump impeller characteristics.

Conflicts of Interest: The authors declare no conflicts of interest.

References

1. Frazier, W.E. Metal Additive Manufacturing: A Review. *J. Mater. Eng. Perform.* **2014**, *23*, 1917–1928. [[CrossRef](#)]
2. Gebisa, A.W.; Lemu, H.G. A case study on topology optimized design for additive manufacturing. *IOP Conf. Ser. Mater. Sci. Eng.* **2017**, *276*, 12–26. [[CrossRef](#)]
3. Kladovasilakis, N.; Charalampous, P.; Tsongas, K.; Kostavelis, I.; Tzovaras, D.; Tzetzis, D. Influence of Selective Laser Melting Additive Manufacturing Parameters in Inconel 718 Superalloy. *Materials* **2022**, *15*, 1362. [[CrossRef](#)] [[PubMed](#)]
4. Kladovasilakis, N.; Charalampous, P.; Tsongas, K.; Kostavelis, I.; Tzetzis, D.; Tzovaras, D. Experimental and Computational Investigation of Lattice Sandwich Structures Constructed by Additive Manufacturing Technologies. *J. Manuf. Mater. Process.* **2021**, *5*, 95. [[CrossRef](#)]
5. Koltsakidis, S.; Koidi, V.; Tzimtzimis, M.; Lappas, A.A.; Heracleous, E.; Tzetzis, D. Influence of Binder Concentration in Zeolitic ZSM-5/Bentonite 3D Printed Monoliths Fabricated Through Robocasting for Catalytic Applications. *Int. J. Adv. Manuf. Technol.* **2023**, *126*, 259–271. [[CrossRef](#)]
6. Zoumaki, M.; Mansour, M.T.; Tsongas, K.; Tzetzis, D.; Mansour, G. Mechanical Characterization and Finite Element Analysis of Hierarchical Sandwich Structures with PLA 3D-Printed Core and Composite Maize Starch Biodegradable Skins. *J. Compos. Sci. Vol.* **2022**, *6*, 118. [[CrossRef](#)]
7. Assael, M.J.; Antoniadis, K.D.; Metaxa, I.; Tzetzis, D. Measurement of the Enhancement of the Thermal Conductivity of an Epoxy-Resin Polymer when Reinforced with Glass Fibres and/or Carbon Multi-Walled Nanotubes. *J. Chem. Eng. Data* **2009**, *54*, 2365–2370. [[CrossRef](#)]
8. Tzetzis, D.; Hogg, P.J. Bondline Toughening of Vacuum Infusion Composite Repairs. *Compos. Part A Appl. Sci. Manuf.* **2006**, *37*, 1239–1251. [[CrossRef](#)]
9. Joosten, M.W.; Neave, M.B.; Rider, A.N.; Varley, R.J. 3D printed continuous fibre composite repair of sandwich structures. *Compos. Struct.* **2022**, *290*, 115518. [[CrossRef](#)]

10. Crump, S.S. Apparatus and Method for Creating Three-Dimensional Objects. U.S. Patent 5,121,329, 1992.
11. Crump, S.S. Modeling Apparatus for Three-Dimensional Objects. U.S. Patent 5,340,433, 1994.
12. Kladovasilakis, N.; Tsongas, K.; Tzetzis, D. Mechanical and FEA-Assisted Characterization of Fused Filament Fabricated Triply Periodic Minimal Surface Structures. *J. Compos. Sci.* **2021**, *5*, 58. [CrossRef]
13. Yongnian, Y.; Shengji, L.; Zhang, R.; Feng, L.; Rendong, W.; Qingping, L.; Zhou, X. Rapid Prototyping and Manufacturing Technology: Principle, Representative Technics, Applications, and Development Trends. *Tsinghua Sci. Technol.* **2009**, *14* (Suppl. S1), 1–12.
14. Gibson, I.; Rosen, D.W.; Stucker, B. *Additive Manufacturing Technologies*, 1st ed.; Springer: New York, NY, USA, 2010. [CrossRef]
15. Cella, L. Pump Materials. 22 July 2022. Available online: <https://www.pumpindustry.com.au/pump-materials-part-1/> (accessed on 12 February 2024).
16. Lee, D.-I.; Lim, H.-C. Erosion-corrosion damages of water-pump impeller. *Int. J. Automot. Technol.* **2009**, *10*, 629–634. [CrossRef]
17. Vazdirvanidis, A.; Pantazopoulos, G.; Rikos, A. Corrosion investigation of stainless-steel water pump components. *Eng. Fail. Anal.* **2017**, *82*, 466–473. [CrossRef]
18. Khalid, Y.A.; Sapuan, S.M. Wear analysis of centrifugal slurry pump impellers. *Ind. Lubr. Tribol.* **2007**, *59*, 18–28. [CrossRef]
19. Sun, J.; Chen, S.; Qu, Y.; Li, J. Review on stress corrosion and corrosion fatigue failure of centrifugal compressor impeller. *Chin. J. Mech. Eng.* **2015**, *28*, 217–225. [CrossRef]
20. Pavlovic, A.; Šljivić, M.; Kraišnik, M.; Ilić, J.; Anic, J. Polymers in additive manufacturing: The case of a water pump impeller. *FME Trans.* **2017**, *45*, 354–359. [CrossRef]
21. Fernández, S.; Jiménez, M.; Porras, J.; Romero, L.; Espinosa, M.M.; Domínguez, M. Additive Manufacturing and Performance of Functional Hydraulic Pump Impellers in Fused Deposition Modelling Technology. *J. Mech. Des.* **2016**, *138*, 024501. [CrossRef]
22. Andres, N.S. Development of Solar-Powered Water Pump with 3D Printed Impeller. *Open Eng.* **2020**, *11*, 249–253. [CrossRef]
23. Kladovasilakis, N.; Kontodina, T.; Charalampous, P.; Kostavelis, I.; Tzetzis, D.; Tzovaras, D. A case study on 3D scanning, digital reparation and rapid metal additive manufacturing of a centrifugal impeller. *IOP Conf. Ser. Mater. Sci. Eng.* **2021**, *1037*, 012018. [CrossRef]
24. Jayawardane, H.; Davies, I.J.; Gamage, J.R.; John, M.; Biswas, W.K. Additive Manufacturing of Recycled Plastics: A ‘Techno-eco-efficiency’ Assessment. *Int. J. Adv. Manuf. Technol.* **2022**, *126*, 1471–1496. [CrossRef]
25. Rajenthirakumar, D.; Jagadeesh, K.A. Analysis of interaction between geometry and efficiency of impeller pump using rapid prototyping. *Int. J. Adv. Manuf. Technol.* **2009**, *44*, 890–899. [CrossRef]
26. Selamat, F.E.; Iskandar, W.H.; Izhan, W. Design and Analysis of Centrifugal Pump Impeller for Performance Enhancement. *J. Mech. Eng.* **2018**, *5*, 36–53.
27. Yadav, K.K.; Mendiratta, K.; Gahlot, V. Optimization of the Design of Radial Flow Pump Impeller through CFD Analysis. *Int. J. Res. Eng. Technol.* **2016**, *5*, 157–161.
28. Rajendran, S.; Purushothaman, K. Analysis of a centrifugal pump impeller using ANSYS-CFX. *Int. J. Eng. Res. Technol.* **2012**, *1*, 1–6.
29. Muttalli, R.S.; Agrawal, S.; Warudkar, H. CFD Simulation of Centrifugal Pump Impeller Using ANSYS-CFX. *Int. J. Innov. Res. Sci. Eng. Technol.* **2014**, *3*, 15553–15561. [CrossRef]
30. Adiaconitei, A.; Vintila, I.S.; Mihalache, R.; Paraschiv, A.; Frigioescu, T.; Vladut, M.; Pambaguan, L. A Study on Using the Additive Manufacturing Process for the Development of a Closed Pump Impeller for Mechanically Pumped Fluid Loop Systems. *Materials* **2021**, *14*, 967. [CrossRef] [PubMed]
31. Spectrum FDM Filament PA6-CF15 Technical Specification Data. Available online: https://spectrumfilaments.com/wp-content/uploads/2022/05/en_tds_spectrum_pa6_cf15.pdf (accessed on 10 March 2024).
32. BS EN 10002-1:1990; Tensile Testing of Metallic Materials—Method of Test at Ambient Temperature. British Standards Institution: London, UK, 2001.
33. TreeD FDM Filament PPS-CF15 Technical Specification Data. Available online: https://treedfilaments.com/datasheets/tech/TDS_PPSCF.pdf (accessed on 10 March 2024).
34. Oliver, W.; Pharr, G. An improved technique for determining hardness and elastic modulus using load and displacement sensing indentation experiments. *J. Mater. Res.* **1992**, *7*, 1564–1583. [CrossRef]
35. Tsongas, K.; Tzetzis, D.; Karantzalis, A.E.; Baniias, G.; Ahmadkhaniha, D.; Zanella, C.; Matikas, T.E.; Bochtis, D. Microstructural, Surface Topology and Nanomechanical Characterization of Electrodeposited Ni-P/SiC Nanocomposite Coatings. *Appl. Sci.* **2019**, *9*, 2901. [CrossRef]
36. Mansour, M.; Tsongas, K.; Tzetzis, D.; Antoniadis, A. Mechanical and Dynamic Behavior of Fused Filament Fabrication 3D Printed Polyethylene Terephthalate Glycol Reinforced with Carbon Fibers. *Polym. Plast. Technol. Eng.* **2018**, *57*, 1715–1725. [CrossRef]
37. Mansour, M.; Tsongas, K.; Tzetzis, D. 3D Printed Hierarchical Honeycombs with Carbon Fiber and Carbon Nanotube Reinforced Acrylonitrile Butadiene Styrene. *J. Compos. Sci.* **2021**, *5*, 62. [CrossRef]

Disclaimer/Publisher’s Note: The statements, opinions and data contained in all publications are solely those of the individual author(s) and contributor(s) and not of MDPI and/or the editor(s). MDPI and/or the editor(s) disclaim responsibility for any injury to people or property resulting from any ideas, methods, instructions or products referred to in the content.